Acta Materialia 274 (2024) 119988

Contents lists available at ScienceDirect

Acta Materialia

journal homepage: www.elsevier.com/locate/actamat

Full length article

Small-scale functional fatigue of a Ni-Mn-Ga Heusler alloy

Adnan Fareed [a], Julian M. Rosalie [a], Satyakam Kar [b,c], Sebastian Fähler [c], Robert Maaß [a,d,e,*]

[a] Federal Institute of Materials Research and Testing (BAM), Unter der Eichen 87, Berlin 12205, Germany
[b] Leibniz IFW Dresden, Institute for Metallic Materials, Helmholtzstr. 20, Dresden 01069, Germany
[c] Helmholtz-Zentrum Dresden-Rossendorf, Bautzner Landstraße 400, Dresden 01328, Germany
[d] Department of Materials Science and Engineering, University of Illinois at Urbana-Champaign, Urbana, IL 61801, USA
[e] Department of Materials Engineering, Technical University of Munich, 85748 Garchingen, Germany

ARTICLE INFO

Keywords:
Shape-memory alloys
Functional fatigue
Ni-Mn-Ga
Superelasticity

ABSTRACT

Functional fatigue of shape-memory alloys is a considerable threat to the reliable service of actuation devices. Here, we demonstrate the essentially degradation-free cyclic phase-transformation behavior of Ni-Mn-Ga microcrystals up to one million stress-driven superelastic cycles. Cyclic dissipation amounts to about 1/5 of the bulk counterpart and remains unaffected during cycling, even after the introduction of dislocation structures via plastic straining. Plastic yielding and the transformation stress largely exceed the known bulk values. However, the transformation-stress is found to depend on plastic pre-straining, which suggests that the size-affected transformation stress is sensitive to the initial defect structure and that it can be tuned by a targeted introduction of dislocations. These findings demonstrate the high suitability of Ni-Mn-Ga as a robust shape-memory alloy in small-scale functional device engineering.

1. Introduction

Shape-memory alloys (SMAs) are indispensable in modern engineering design due to their large reversible strains that make them ideal for actuation [1–3]. Fundamentally relying on a stress- or temperature-driven phase change between a high temperature austenitic and a low temperature martensitic phase, different bulk systems have in the past been investigated with respect to their maximum reversible strain [4–7], compositional superelastic tuning [8,9], or stress induced transformation behavior [10,11]. In bulk model systems, as well exemplified with Ni-Ti, fundamental investigations in the quasi-static domain have brought to light the detailed phase-transformation pathways that may reveal intermediate meta-stable phases [12,13] or early formation of residual martensite [14].

Whilst microstructural changes during quasi-static stress-driven cycling and also functional fatigue in bulk systems are well understood, strongly size-dependent mechanical [15] and functional [16,17] behavior may arise at the micro- or nano-scale. In the wake of continued size reduction, which leads to micro- and nano-electro-mechanical (MEMS/NEMS) systems, such length-scale effects need to be quantified in detail to ensure reliable small-scale actuation. Returning to the example of Ni-Ti, Frick and co-workers firstly demonstrated a complete loss of superelasticity [18], pronounced orientation effects, and the formation of residual martensite pockets even after a single stress-driven transformation cycle [19]. In contrast to such plasticity-driven deterioration of the strain reversibility, Cu-Al-Ni or Au-Cu-Zn SMAs retain their superelastic behavior even at sub-micrometer scales, which has been attributed to larger differences between the critical phase-nucleation stress and the stress required for plastic yielding compared to Ni-Ti [20]. In addition, the phase-transformation stress in these alloy systems exhibits a marked size effect, meaning that extrinsic sample sizes need to be considered in MEMS and NEMS design.

The aforementioned size-dependent properties of SMAs relate to their quasi-static response and superelastic switching of at most a few phase-transformation cycles. However, any reliable application in actuation will require a large cycle number, during which functional fatigue has to be assessed at small length scales. Mechanical multi-cycle superelasticity has indeed been investigated for Cu-Al-Ni [21], Cu-Al-Be [22], and Ni-Mn-Ga [23] for some thousand load-unload cycles, whereas functional degradation including the underlying microstructural mechanisms up to a million load-unload cycles have been investigated in great detail only for nanocrystalline Ni-Ti [24]. The latter case reveals a strong sensitivity to transformation-induced dislocations that lead to

* Corresponding author at: Federal Institute of Materials Research and Testing (BAM), Unter der Eichen 87, Berlin 12205, Germany.
E-mail address: robert.maass@bam.de (R. Maaß).

https://doi.org/10.1016/j.actamat.2024.119988
Received 7 February 2024; Received in revised form 3 May 2024; Accepted 6 May 2024

incomplete phase reversibility, cause surface extrusions, and promote surface shear-cracks, all of which results in a continued decrease in the residual strain upon cycling and a transformation-stress reduction that plateaus at about 10^4 cycles [24].

Here, we focus on the Ni-Mn-Ga ferromagnetic Heusler system, which has an $L2_1$ ordered lattice, and which exhibits both mechanical and magnetic phase-transformations. This combination makes Ni-Mn-Ga an ideal multifunctional SMA [25], combining high-stroke actuations [26–28], multicaloric effects [29,30], and thermomagnetic energy harvesting [31,32]. Produced now as thin films with the austenitic phase stable at room temperature [33], it has become possible to conveniently interrogate the structural stability and its superelastic response at reduced length scales [33,34]. In contrast to superelastic cycling of micro- or nanocrystals extracted from bulk poly- or single crystals, the film deposition approach offers to directly characterize Ni-Mn-Ga at the application scale and with its processing-dependent microstructural characteristics. For example, a strong increase in the stress scale and an incomplete reversibility of the incipient austenitic-martensitic phase transformation has been reported for sub-micrometer films on MgO substrates [34], which hints at length-scale dependent dissipation. In particular in multi-variant transformations, pockets of residual martensite in combination with local deformation structures are expected to cause functional fatigue due to an increasingly strained habit plane between austenite and martensite. With the additional revelation that sputter-deposited Ni-Mn-Ga thin films may contain premartensitic domains [35], having a hierarchical microstructure of nano- and mesoscopic twin boundaries [36], the overall phase-transformation cycling, its dissipative properties, and possible microstructural evolutions during continued phase-switching need to be assessed.

To this end, we subject here cylindrical austenitic Ni-Mn-Ga microcrystals to compressive fatigue at room temperature for up to 10^6 consecutive load-unloading cycles. We find that the superelastic response exhibits at most a 2–3% reduction in strain magnitude and that hysteretic losses are approximately five times smaller than at the bulk scale, irrespective of cycle number, grown-in dislocation structures, premartensitic domains, or introduced plastic pre-strains. Complementary transmission electron microscopy reveals no indications of any residual martensite even in microcrystals with significant dislocation structures. As such, micro-scale Ni-Mn-Ga demonstrates a strong size effect in the austenite-martensite transformation stress but is essentially loss-free and undergoes superelastic cycling for up to 10^6 cycles without any functional fatigue.

2. Experimental details

Single crystalline Ni-Mn-Ga films with a thickness of 4.8 μm were fabricated using DC magnetron sputtering on single-crystal MgO (001) substrate with a 150 nm epitaxial Cr-buffer layer, as described in detail in Refs. [27,35]. The Cr buffer layer is used to enhance the adhesion between the film and substrate, to promote a smooth surface of the film by covering substrate defects, and to mitigating stress relaxation at the interface [35]. To ensure a high degree of chemical ordering and epitaxial growth, the substrate temperature was kept at 673 K during deposition. Following film processing, the composition of the film was determined via energy dispersive x-ray spectroscopy (EDX) using a $Ni_{50}Mn_{25}Ga_{25}$ standard, which yielded a film composition of $Ni_{51.3}Mn_{21.7}Ga_{27}$ with an accuracy below 1 at.%. The sample's phase-transformation behavior was examined using a vibrating sample magnetometer (VSM, Quantum Design-VERSALAB) with a constant magnetic field of 0.01 T in the temperature range of 200–400 K and with a heating-cooling rate of 2 K/min. The magnetic field was applied in-plane along the MgO [100]-direction. Evaluated from heating, the VSM trace returned an austinite starting transformation temperature, A_s, of 180 K and a finishing temperature, A_f, of 222 K, whereas the corresponding martensite starting and finishing temperatures during cooing were found to be $M_s = 214$ K, and $M_f = 175$ K, respectively. A Philips X'Pert four-cycle x-ray setup equipped with a Cu tube and a primary Ge monochromator was used to perform reciprocal space mapping of (206) Ni-Mn-Ga, (103) Cr, (224) MgO substrate reflections to obtain their *in-plane* lattice constants. The obtained values are 5.822 Å (Ni-Mn-Ga), 2.890 Å (Cr), and 4.214 Å (MgO).

Following the standard annular ion milling procedure [37], free standing cylindrical microcrystals were prepared using focused ion beam (FIB, FEI Quanta). Given the epitaxial growth conditions, all microcrystals had a vertical axis along the Ni-Mn-Ga [001]-direction and a height of 4.8 μm, set by the film thickness. A nominal diameter of 2 μm was targeted and each microcrystal was placed inside a circular trench with a 20 μm diameter. To reduce microcrystal taper and to minimize possible ion-beam damage [38,39], a final milling current of 30 pA at a voltage of 30 keV was used. After sample milling, scanning electron microscopy (SEM) was used to quantify the column taper using $= \tan^{-1}((r_1 - r_2)/h)$, where θ is the taper angle, h the column height, and r_1 and r_2 are the bottom and top radii. The used procedure resulted in cylindrical microcrystals with an aspect ratio of 4.8/2 and final column tapers of $\theta < 2^\circ$.

Micro-mechanical testing in compression was carried out using a Bruker-Hysitron TI 980 nanoindentation platform, equipped with a 10 μm diamond flat punch tip. Quasi-static testing was done at room temperature and as a function of temperature at a strain rate of $3 \times 10^{-3}\,s^{-1}$, whereas dynamical testing at 0.5 Hz was only conducted at room temperature. Cyclic loading in compression was done at a maximum stress of $\sigma_{max} = 943$ MPa, a minimum stress of $\sigma_{min} = 3$ MPa, a stress amplitude of $\sigma_a = 470$ MPa, and a stress ratio R of 0.003 (all indicated in Fig. 4a and much similar to Ref. [40]). All experiments were conducted in displacement-controlled mode. Pre- and post-deformation SEM imaging was pursued to document deformation morphologies and during cyclic testing the samples were imaged every 200 000 cycles, if the total load cycles exceeded this value. Furthermore, transmission electron microscopy (TEM, JEOL 2200FS) was used to characterize the microstructure of the as-prepared, quasi-statically deformed, and fatigued columns. To this end, a cross-sectional TEM foil of the full column was made via the FIB-based lift-out method. Scanning-transmission mode (STEM), bright-field (BF) imaging, and selected-area diffraction (SAD) were used during TEM to quantify the defect structure along the vertical microcrystal axis.

3. Results

3.1. As-prepared Ni-Mn-Ga film and microcrystals

Prior to micro-mechanical testing and the quantification of any functional fatigue in response to cyclic mechanical switching between austenite and martensite, the initial microcrystal microstructure is examined using TEM. Fig. 1a shows a cross-sectional BF-STEM image of an as-prepared microcrystal. At the bottom of the column, the thin Cr buffer and the MgO substrate are visible. Surrounding the column, FIB-deposited Pt is seen, which was used to embed and protect the column during TEM sample preparation. Two microstructural contrasts are seen within the column, being (i) a horizontally aligned wavy structure, and (ii) vertically oriented lines. The latter are dislocations, that must arise during single-crystal film growth and that therefore are classified as threading dislocations. At this point qualitatively, and later quantified, their density reduces from bottom to top of the microcrystal. This is the expected dislocation gradient [41,42] arising from non-perfect lattice--parameter matches seen in deposited films, here originating from mismatches between the Ni-Mn-Ga austenite and the Cr-buffer in the (001)-plane. Whilst small, the lattice misfit amounts to approximately 3.01% between the Cr buffer and the MgO, whereas 0.7% is found for the misfit between the Cr buffer and the Ni-Mn-Ga film from the epitaxial growth relation [35], using the (in-plane) lattice parameters obtained by reciprocal space mapping.

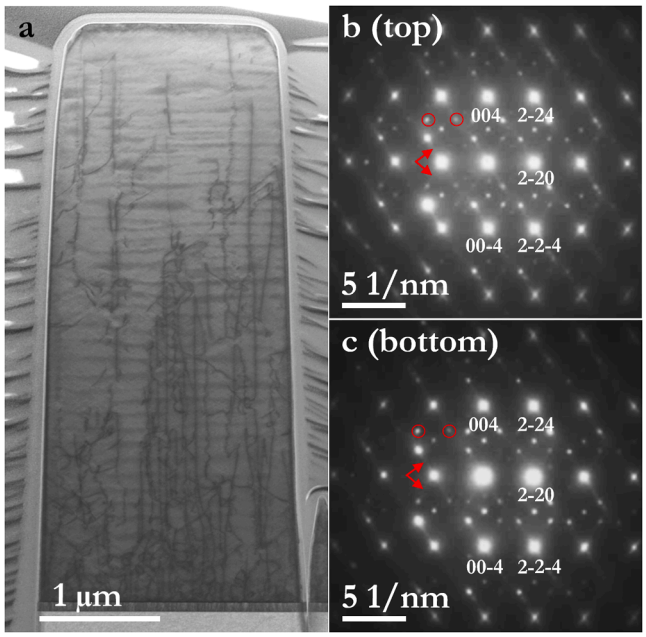

Fig. 1. (a) Bright-field STEM image of an as-prepared microcrystal. The horizontal wavy lines are indicative of a premartensitic structure [35]. A network of primarily vertically aligned threading dislocations is also visible, with a higher dislocation density near the microcrystal base. SAD patterns from the upper and lower region of the microcrystal are shown in (b) and (c), respectively. Red arrows in (b) and (c) mark diffuse streaks originating from the premartensite. Two out of four low intensity satellite spots from the premartensite are encircled in red in the SAD patterns. (For interpretation of the references to colour in this figure legend, the reader is referred to the web version of this article.)

The wavy horizontal contrast is a clear indication for an extended premartensitic microstructure, which we recently characterized in detail in Ref. [35] and that has been reported for a variety of other SMAs, including Ni-Al [43,44], Ni-Ti [45,46], and Fe-Pd [47,48]. The premartensite is characterized by a small tetragonal distortion that hardly deviates from the cubic symmetry of the austenitic phase. Similar to other modulated structures like 10 M and 14 M, 6 M can be explained by the adaptive concept, but with a very low tetragonal distortion [49–51].

The SAD patterns in Fig. 1b and 1c are indexed for imaging along the [110]-zone-axis, with the axial direction of the microcrystal in the [001]-direction. The high-intensity spots in the diffraction pattern identify the cubic Ni-Mn-Ga austenite. The red arrows indicate streaks that are observed around the main diffraction spots and enclose approximately 63.5°, which are perpendicular to the crosshatch striations that can be observed in the bright-field STEM image. In addition, four low intensity satellite spots are found around each main diffraction peak, two of them encircled in red in both Fig. 1b and 1c. These satellites have been investigated in our previous work, where dark field TEM imaging linked them to the alternating bright and dark horizontal wavy band features, revealing the premartensitic state in the film matrix [35]. Using the premartensitic diffraction peaks for dark field imaging, the premartensite can be highlighted and its volume fraction in the as-prepared material can be estimated. This yields a premartensitic volume fraction of 0.75±0.05, where the error is due to uncertainties in the exact contrast thresholding used during dark field image analysis. The as-prepared microcrystals can consequently be considered austenite with a considerable volume fraction already on its path towards the lower-temperature martensite phase.

Considering the aim of characterizing the small-scale mechanical response and potential functional fatigue in response to mechanically-induced phase-cycling, as a first step we pay attention to FIB-induced surface damage – a topic that received considerable attention in size-affected crystal plasticity [52]. Indeed, FIB can lead to ion-damage induced lattice strain gradients [53], give rise to surface damage and alloying within the first tens of nm of the crystal [54,55], and significantly reduced yield stresses relative to the non-FIBed crystal [39,56]. These effects arise from ion-implantation and point-defect formation [39]. At sufficient high mobility, which is the case in soft and low melting point metals, these point defects can collapse into loops that in turn contribute to a FIB-milling-dependent line-defect population.

Whilst not being able to exclude or track nano-scale lattice modifications in the microcrystal surface in-detail, a wet-chemical etching methodology is pursued that allows uniform removal of the crystal surface. In a first step, an as-prepared film was etched at room temperature with 1.25%HCl + 37%HNO_3 + H_2O to determine the film thickness reduction rate under these conditions. Subsequently, a film containing a series of microcrystals was etched for 3 min to remove a targeted surface layer of approximately 70 nm [57]. Successful etching was verified with SEM via the measurements of sample dimensions and the surface morphology. After etching, the micromechanical response of as-FIBed and FIBed and wet-echted specimen was compared (Fig. 2).

Both an as-FIBed and a FIBed and etched sample was loaded uniaxially to a maximum force of 2 mN, which equates to ca. 800 MPa. 20 load-unload cycles are applied to both sample states. As can be seen in Fig. 2, all load cycles fall within the precision of the experiment well on top of each other, but minor differences in the stress-hysteresis and maximum strain are present. The latter is attributed to the typical uncertainties in sample length determination under tilted SEM imaging conditions, where 5 nm measurement variations easily lead to the observed 0.2% strain difference. With this assessment, it is therefore concluded that any potential FIB-induced surface damage does not affect the superelastic response of the Ni-Mn-Ga-alloy. In the following we will hence only consider as-FIBed microcrystals.

Fig. 3 directly compares the mechanical loading-unloading response of a $Ni_{52}Mn_{24.4}Ga_{23.6}$ bulk single crystal [6] and pristine microcrystals, all stressed along the [100]-direction. Compared at room temperature, the phase-transformation induced softening of the microcrystals begins at about 2% strain (~96 nm displacement), with a less-distinct martensitic transition than at the bulk scale that we in part ascribe to the premartensitic structures in the microcrystals. However, a proper comparison of the transformation stress requires considering the temperature difference between the testing temperature and the martensitic

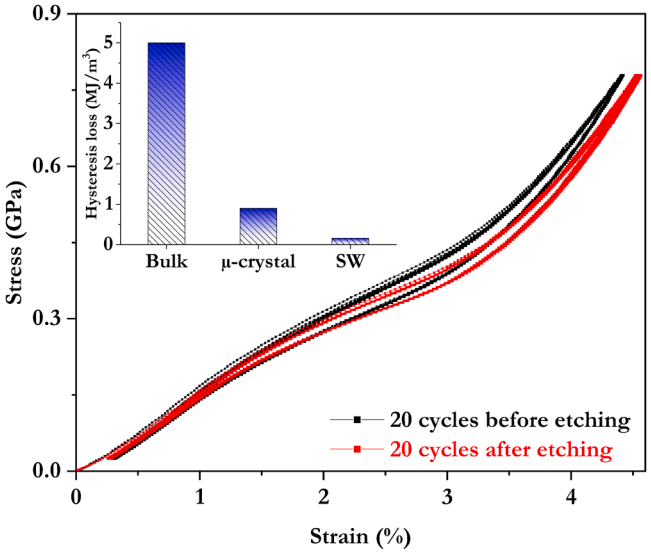

Fig. 2. Stress-strain behavior of an as-FIBed and a FIBbed and subsequently wet-etched microcrystal. In each case, twenty superelastic cycles are shown. The inset shows the stress-strain hysteresis loss of the microcrystals (µ-crystal) in comparison their bulk counterpart [6] and relative to a silicon wafer (SW) material. Distinctly lower losses are seen at the micron-scale.

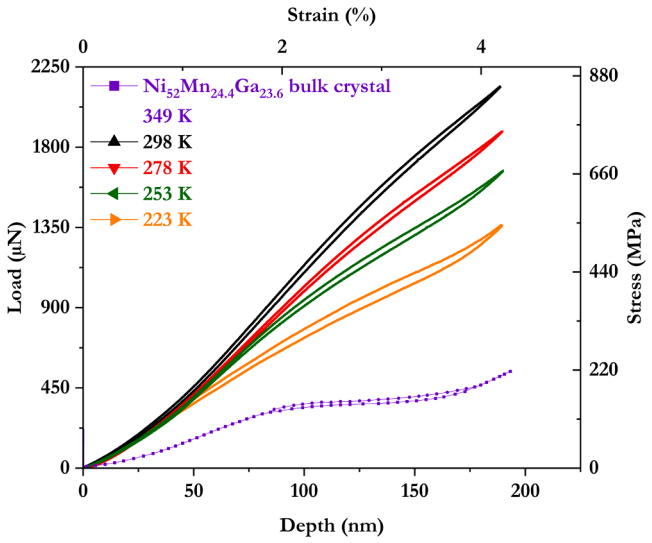

Fig. 3. Load-displacement response of the microcrystals at four different temperatures in comparison to the bulk response measured at 349 K (M_s = 310 K). Bulk crystal data is taken from Ref. [6]. With decreasing testing temperature of the microcrystals (M_s = 207 K and A_s = 218 K along the [100]-direction), the transformation stress decreases but remains much larger than at the bulk scale.

transformation temperature (M_s) of both the microcrystal and the bulk alloy. For the bulk crystal that was tested at 349 K, a martensitic transformation temperature of 310 K was reported, whereas the microcrystals have an M_s = 207 K. With decreasing testing temperature of the microcrystals, that is a decreasing $T_{exp} - M_s$, one therefore expects a stress-scale reduction and a gradual approach to the bulk stress-strain curve, as can be seen in Fig. 3. Relying on the second derivative of the microcrystal data in Fig. 3, the transformation stress at each temperature can be determined to 462 MPa (298 K), 340 MPa (278 K), 220 MPa (253 K), and 110 MPa (223 K). For the case of the microcrystals, it is now meaningful to apply the Clausius-Clapeyron equation

$$\frac{d\sigma}{dT} = \left(\frac{dH * \rho}{M_s * \varepsilon}\right)(T_{exp} - M_s) \quad (1)$$

where dH is the change in enthalpy (taken as 6.1 Jg^{-1} from Ref. [58]), ρ is the density, ε is the strain (taken from the micro-compression), and T_{exp} the experimental deformation temperature. Inserting the appropriate values for the microcrystals yields $\Delta\sigma^{\langle 100\rangle}/\Delta T$ = 5.7 MPa /K, which compares to about 3.5 MPa/K at the bulk scale [6]. With this value at hand, a direct comparative estimate of the microcrystal transformation stress relative to the bulk value can be made. Indeed, at $T_{exp} - M_s$ = 16 K one obtains a transformation stress of 110 MPa for the microcrystals and 60 MPa for the bulk counterpart using data from Ref. [6]. This estimate is subjected to some variance due to the unknown appropriate enthalpy value for the microcrystals, but clearly demonstrates a size-affected transformation stress.

In addition to this marked difference in transformation stress between the microcrystal and the bulk material at room temperature, it is instructive to compare the enclosed area of the hysteretic response during the first loading cycle. The bulk crystal exhibits a stress-strain hysteresis enclosing ca. 5 MJ/m^3, whereas the microcrystal absorbs approximately 0.45 MJ/m^3 at room temperature, and 0.5 MJ/m^3, 0.55 MJ/m^3, and 0.7 MJ/m^3 with decreasing temperature. This strong difference has to be put into perspective relative to the instrumental setup damping that amounts to ca. 0.16 MJ/m^3, as determined by cyclic loading on a Si single crystalline wafer piece. The inset in Fig. 2 summarizes these values.

3.2. Cyclic response and functional fatigue

In anticipation of a large number of superelastic load-unloading cycles in service, the cyclic switching behavior of the Ni-Mn-Ga microcrystals is now investigated in compression at room temperature. The inset in Fig. 4a exemplifies these cyclic loading conditions with data for a sample cycled 10^3 times. Fig. 4a shows the load-unloading behavior of different microcrystals that have experienced 10^3, 10^5, and 10^6 total cycles, respectively. For better readability, the data of each crystal was shifted along the abscissa. In each case, the first and the last load-unloading cycle is plotted, demonstrating the superelastic robustness of the reversible strain magnitude, which amounts to ca. 4.25% in all cases. Despite this, a small reduction in switching strain can be discerned after 10^6 cycles. To quantify this loss in more detail, both the reversible strain magnitude and the enclosed hysteresis envelop is analyzed as a function of cycle number, N.

As summarized in Fig. 4b via the relative strain magnitude, no microcrystal experienced any cyclic strain reduction for the first 10,000 cycles, whereas small drops of the order of 2–3% are observed at ~5 × 10^4 and 8 × 10^5 cycles. Similarly, the enclosed envelop area reveals virtually no indication for increasing internal dissipation during mechanical switching. Of the three fatigued cases in Fig. 4b, the microcrystal of 10^6 cycles was evaluated at every 2 × 10^5 cycles. Indeed, the damped energy is very small and of the order of 0.85–0.9 MJ/m^3 for 10^3, 10^5, and 10^6 cycles, which compares very well to the as-prepared microcrystal and therefore remains about four times larger than the base-reference of the Si wafer (inset in Fig. 2). This underlines that (i) dissipation in the Ni-Mn-Ga microcrystals is significantly larger than the experimental resolution and that (ii) the dissipation during repeated phase transformations remains at least five times smaller than in the corresponding bulk case and is essentially independent of N.

Complementary to the mechanical characterization, SEM was used to monitor the sample dimensions and surface morphology as a function of cycling for the case of $N = 10^6$. Every 200 000 cycles, the specimen was imaged from the same viewing direction, of which the images for $N = 0$, and $N = 10^6$ are shown as insets in Fig. 4b. No indications of plastic deformation or top-surface damage can be resolved, which underlines the essentially loss-free cyclic microcrystal behavior. We therefore conclude that no residual martensite has been accumulated even after one million mechanically-induced phase transformations. Subsequent TEM investigations presented in Section 3.4 will substantiate this intermediate conclusion.

3.3. Superelastic response and functional fatigue after pre-deformation

3.3.1. Superelasticity in response to plastic deformation

Having demonstrated the practically degradation- and loss-free cyclic stress-driven phase-transformation behavior, we now consider the case of pre-deformation and its effect on the cyclic switching behavior. In each case, uniaxial compression is conducted quasi-statically to a certain total plastic strain, followed by stress-driven phase-transformation cycling to the same maximum stress of 900 MPa as during cyclic fatigue. Fig. 5 summarizes exemplarily a sequence of four consecutive plastic strain increments introduced into the same microcrystal. This stepwise accumulation of plastic pre-strain is required, as the exact plastic strain introduction is not controllable due to the stochastic and intermittent deformation seen after yielding. Indeed, at and beyond yielding (break-away stress) in this size regime, large abrupt strain bursts, also referred to as dislocation avalanches, may unintentionally lead to instantaneous plastic strain of several percent [59,60]. To be able to study the effect of plastic pre-strains of up to ca. 17% on the superelastic response, we therefore pursue the incremental testing procedure as displayed in Fig. 5. Fig. 5 also shows in each case the fully reversible load-unloading response prior to introducing the plastic strain increment, which at the same time represents the superelastic response after the previous deformation cycle.

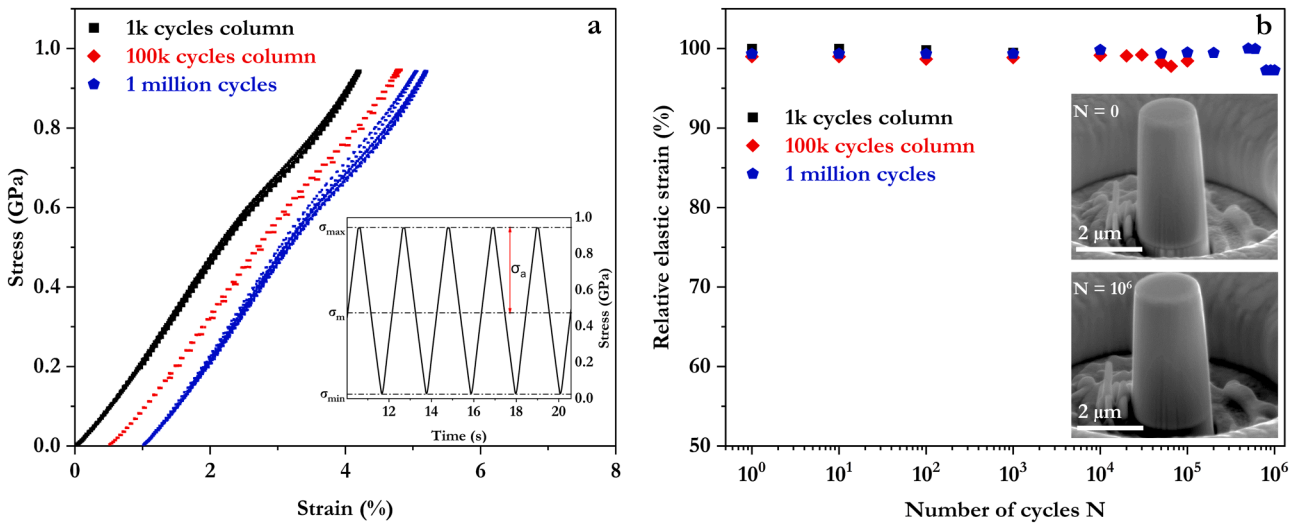

Fig. 4. (a) Stress-Strain curves of cyclic loading for cycle number 10^3, 10^5, and 10^6. The inset in (a) displays a load-time trace example of a sample cycled 10^3 times. (b) Relative elastic strain plotted for three microcrystals subjected to 10^3, 10^5, and 10^6 super-elastic cycles, respectively. The upper inset ($N = 0$) shows a microcrystal before 10^6 super-elastic cycles, whereas the lower inset ($N = 10^6$) displays the same crystal after fatigue testing.

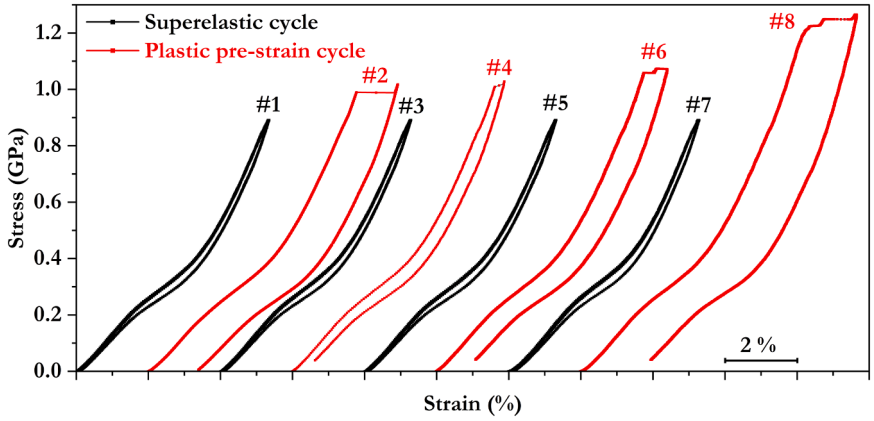

Fig. 5. Examples of a plastic pre-straining sequence, which was pursued to obtain a specific targeted total pre-strain. All curves have been shifted for clarity and are presented in their sequential order from left to right. Superelastic and plastic pre-straining cycle numbers are indicated with numbers. These four plastic deformation cycles represent the first ones towards the total 17% plastic strain contained in Fig. 6. The superelastic response was probed with 10 cycles prior to plastic straining, of which the first cycle is shown for each of the four cases. Superelastic cycling before the next deformation cycle represents therefore the mechanical response after the previous deformation cycle.

Subsequently, the stress-driven phase switching response of the plastically pre-deformed microcrystals is characterized by at least 10 consecutive load-unloading cycles. Fig. 6 summarizes the relative elastic strain recovery as a function of plastic pre-straining for two microcrystals. Despite some scatter, both samples follow the same trend of a gradual decay of the maximum strain recovery relative to the initial value of the undeformed specimen. Phenomenologically, the decaying elastic recovery strain is well approximated by a simple exponential decay function with a decay parameter of 4.4 ± 0.72. Notably, only plastic strains exceeding approximately 6% plastic pre-deformation lead to a reduction in maximum switching strain that exceeds 2.5%, which demonstrates a remarkable robustness of the phase transformation against introduced defect structures. Even after plastic engineering strains as large at 15%, the tested microcrystals still exhibit relative recovery strains of approximately 85% (that is, a ca. 15% reduced recovery strain), where the rate of recovery loss with plastic strain increases strongly with strain accumulation. We note that elastic recovery strains are always evaluated with respect to the actual sample length, meaning the length reduction due to plastic deformation was taken into account.

The inset in Fig. 6 reveals how the recovery strain typically reduces with plastic strain accumulation. For the 10 displayed curves, each of which was obtained after an additional plastic strain increment, much similar to what is shown in Fig. 5, a gradual reduction of the superelastic strain is seen while keeping the targeted maximum stress constant. An arrow located at the peak stresses in the inset in Fig. 6 indicates this gradual superelastic strain reduction. The legend in the inset in Fig. 6 quantifies the reducing superelastic strain for each loading, with the first value in the legend being the total plastic pre-strain (ε_{pl}) and the second value indicating the reversible stain magnitude (ε_{el}). Inspection of the curvatures (first and second derivates) of each curve in the inset of Fig. 6, reveals that the initial concave part reduces with increased plastic pre-strain until only an entirely convex stress-strain response remains for the largest amounts of induced plastic pre-strain, as can be seen in the inset. This change in the superelastic stress-strain response does not lead to a simple linear elastic loading behavior and still exhibits a reversible strain of about 4% even after 17% total plastic strain. Since it is the convex component of the stress-strain response that remains, but the initial concave component is reduced, we interpret this primarily as a loss of the austenite's ability to respond elastically prior to undergoing

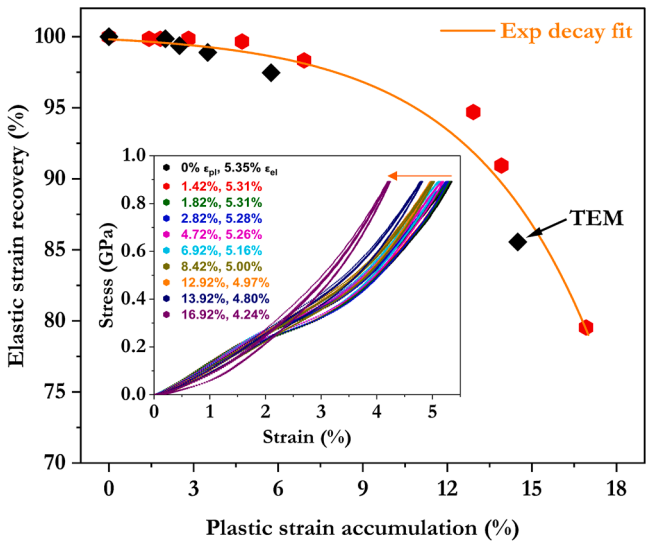

Fig. 6. Relative elastic strain behavior of two microcrystals. An exponential decay describes the strain-recovery loss as a function of plastic pre-strain well. Until ca. 6% plastic pre-strain, the strain-recovery loss remains below 2.5%. The inset displays the stress-strain response after 10 successive plastic strain increments. With increasing plastic strain accumulation, the reversible strain magnitude reduces. This is indicated as an arrow in the inset, and the legend displays in order the imparted plastic pre-strain ε_{pl} followed by the elastic recovery strain ε_{el}.

a phase change. Therefore, the data in the inset of Fig. 6 suggests that the continued accumulation of plastic strain leads to a progressively lower stress at which the martensitic phases transformation is induced. This interpretation would mean that no residual martensite is present after plastic pre-straining. Indeed, later discussed TEM investigations reveal an austenitic microstructure even after plastic pre-straining, supporting our interpretation that irreversible deformation (slip) seems to lower the nucleation stress of the austenite-martensite transformation.

3.3.2. Functional fatigue with addition of plastic response

With the insight that the Ni-Mn-Ga microcrystals can forgive large amount of plastic-pre-straining and still keep their superelastic response, albeit with a strong indication for a reduced elastic contribution from the pure austenite phase, we now investigate the cyclic superelastic behavior for up to 10^5 loading cycles. To this end, small plastic pre-strains of the order of 3% are targeted. Fig. 7a summarizes this approach, where first the loading of the as-prepared microcrystal is assessed, followed by a targeted plastic pre-straining, and finally the superelastic behavior of the deformed samples was verified prior to cyclic loading. In good agreement with the data in Fig. 6, the recovery strain reduces from 100% to 96–97.5% of its original value after 2–3% plastic pre-straining (Fig. 7b).

Following the same procedure as in Section 3.2, the elastic recovery of the microcrystals is tracked as a function of mechanical cycling. The evolution of the pseudo-elastic strain recovery as a function of cycle number is shown in Fig. 7b for four different samples. In all cases, the first large drop in elastic strain recovery is due to the introduced plastic pre-straining, after which a negligible (<1%) or no further reduction of the switching behavior is observed until 10^5 cycles. In direct comparison to the functional fatigue of the as-prepared microcrystals displayed in Fig. 5b, the seen losses less than 1% of the pre-deformed microcrystals is very well comparable. This underlines the robust mechanically induced phase-switching behavior of Ni-Mn-Ga, which remains quantitatively identical even after the introduction of a dislocation structure and localized shear.

3.4. Microstructure of deformed and fatigued microcrystals

To gain further understanding of possible microstructural changes in response to uniaxial deformation and functional fatigue, cross sectional FIBed TEM lamellae were prepared from microcrystals that underwent 10^5 and 10^6 superelastic cycles and from a microcrystal that was strained uniaxially to ca. 15%. Bright field STEM images and corresponding SAD patterns obtained at the top and bottom along the [110]-zone axis of the cyclically loaded microcrystals are shown in Fig. 8. In both cases (10^5 cycles, Fig. 8a–c; 10^6 cycles, Fig. 8d–f) all obtained SAD patterns only reveal the austenitic phase, with additional low-intensity satellite spots corresponding to the premartensitic structure. Since no indications for modulated or non-modulated residual martensite can be identified, only the weak differences in the dislocation network and the tweed structure of the premartensite between the pristine and the mechanically cycled microcrystals can be underlying the small mechanical losses captured in Fig. 4.

A different picture emerges when examining a deformed microcrystal. Fig. 9 displays SAD patterns for the crystal top (Fig. 9a) and

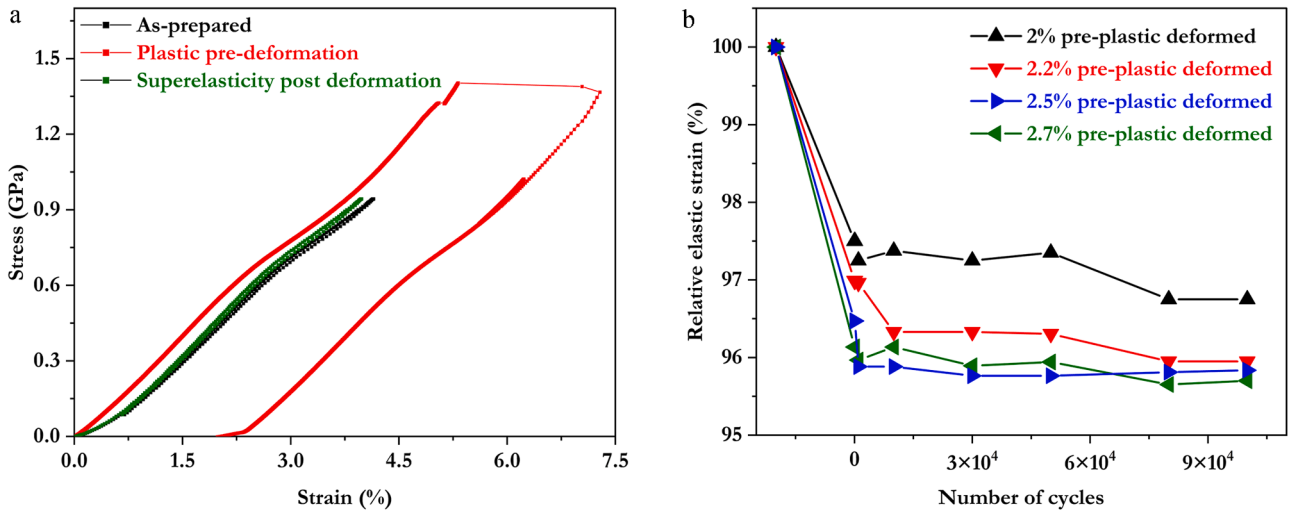

Fig. 7. (a) A superelastic cycle (black, pre-deformation) of an as-prepared microcrystal, followed by a 2% plastic deformation (red, deformation), and the first superelastic loading (green, cycle 1) of a subsequent functional fatigue experiment. (b) Relative elastic strain as a function of fatigue cycle number for four microcrystals with different plastic pre-strains. (For interpretation of the references to colour in this figure legend, the reader is referred to the web version of this article.)

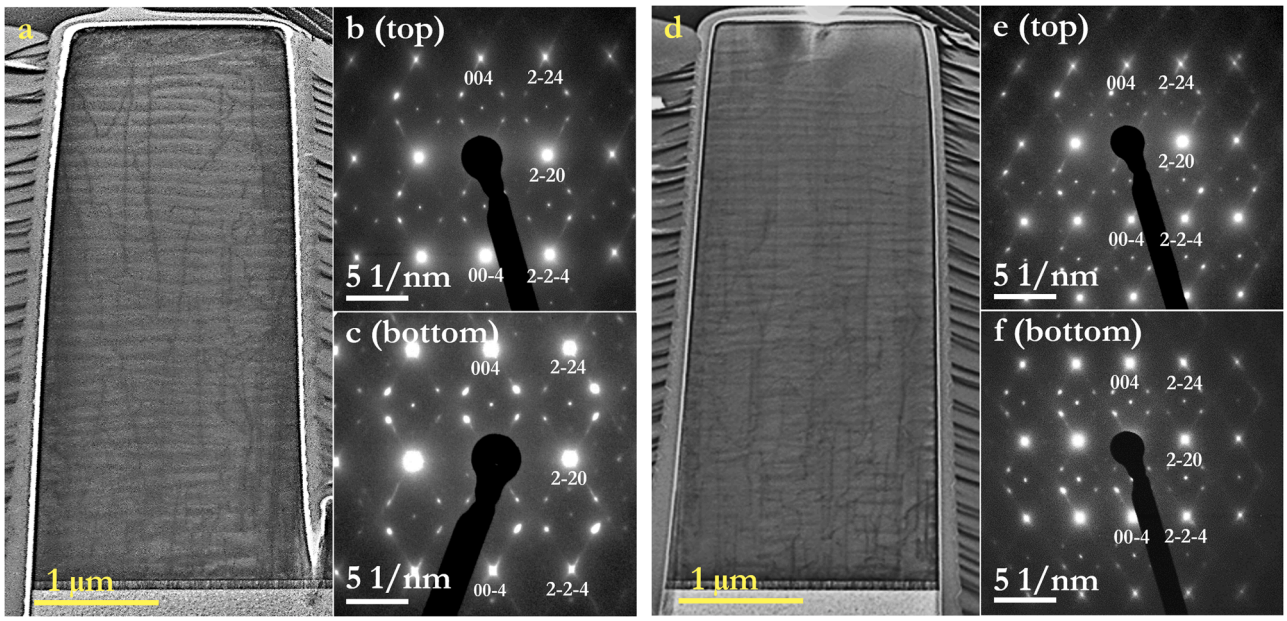

Fig. 8. TEM BF-STEM micrographs of microcrystals after 10^5 (a) and 10^6 (d) cycles. Despite extensive superelastic cycling, the wavy contrast of the premartensite remains in both cases. This is also apparent from the SAD patterns, which show the same features related to the premartensite as depicted in Fig. 1. SAD patterns (b) and (e) are from the upper column parts, and (c) and (f) are from the lower parts of the columns.

bottom (Fig. 9b) with strong diffraction intensity streaking of the main austenite peaks, whereas the relative intensity of the premartensite has reduced. The bright-field STEM image of the microcrystal cross-section reveals distinct differences between the as-prepared or mechanically cycled microstructures, with dislocation and slip signatures in the lower part of the crystal and a contrast at the top that indicates lattice rotations and a dense dislocation network. This deformation signature is typical for microcrystals deformed in compression, where dislocation nucleation and accumulation is known to occur in the specimen near the anvil-sample interface and where the most pronounced rotational gradients emerge at the ends of the column, often coinciding with localized slip [53,61]. In direct comparison to the as-prepared microstructure, the observed as-deposited/grown-in threading dislocation population with the distinct vertical alignment has disappeared after plastic deformation. Despite this accumulation of a deformation structure that is typical for the conducted micro-mechanical tests, still no residual martensite can be identified within the precision of the SAD TEM investigations.

To better quantify the change in dislocation structure in response to superelastic cycling and plastic deformation, the dislocation density along the vertical crystal axis is evaluated using the intercept method. Going from sample top to bottom, the dislocation density is evaluated every 500 nm. Fig. 9d summarized the position-dependent dislocation density along the microcrystal for the as-prepared state, after 10^5 and 10^6 cycles of loading, and selectively for the 15% plastically strained case. In general, crystals that have not been strained plastically do exhibit a gradual reduction of the dislocation density going from bottom to top, which aligns with the expectation of a higher density of threading dislocations due to interfacial constraints during film processing. The crystal that was fatigued for 10^6 cycles evidences a slight hump or local increase in dislocation density close to the top. Whilst not possible to verify, this may explain the mild loss in strain-reversibility observed during cyclic loading in Fig. 4b. Wherever locally quantifiable, the plastically deformed microcrystal reveals either a lower dislocation density or domains of dense networks, which suggests that the previously seen grown-in dislocation network has either been pushed out of the specimen or they are now part of the dense and not quantifiable domains of slip or lattice rotation at the crystal top.

4. Discussion

4.1. Size-affected plastic shear deformation and microscopic slip

Due to the $L2_1$ Heusler structure and its chemical ordering, slip distances smaller than a full translational lattice vector generate antiphase boundaries. Thus, dislocation splitting is energetically favorable, typically leading to four paired $1/4\langle 111\rangle$ partials (partial superlattice dislocations) on {110}-planes, separated by their specific antiphase boundary ribbon. This has for example been studied in detail in Cu_2MnAl or DO_3 ordered Fe_3Si [62,63]. Whilst this indicates high stresses for dislocation motion, slip in the here investigated microcrystals occurs after the inflection point of the superelastic response, meaning that the martensitic phase deforms during plastic pre-yielding (Figs. 5 and 7a). After unloading and phase transformation back to austenite, slip lines on the {110}-planes are indeed observed (Fig. 9a), which also are the expected slip planes in tetragonal martensite. The break-away slip for the martensitic phase is observed in the range between 1.1 and 1.3 GPa, which largely exceeds the reported Ni-Mn-Ga bulk yield-stress that is in the range of 630 MPa [23]. This yield-stress doubling at the micron-scale is in line with expectations based on size-dependent single crystal strengthening that follows a power-law scaling of type $\sigma \sim d^{-n}$, with d being an external length scale and n typically ranges between 0.3 and 0.6 [64]. With this increase of the stress required to induce plastic shearing in the formed martensite, naturally a larger stress range emerges during which stress-driven cycling is possible. Whilst no systematic size-dependent study was conducted here, these findings suggest that the superelastic response limit of Ni-Mn-Ga increases with decreasing sample size, being in agreement with singular observations for Cu-Al-Ni [65].

Given a lower transformation stress in comparison to the high stresses for glide initiation in $L2_1$-ordered Ni-Mn-Ga, slip in the austenitic phase is not expected. This is indeed supported by the TEM micrographs revealing no evidence of dislocation activity after superelastic cycling (Figs. 1 and 8). Slip and therefore a disruption of the local chemical order emerges first at high enough stresses in the martensitic phase. This is distinctly different to SMAs with lower Peierls barriers, such as in B2-ordered Ni-Ti [66]. In these cases, also partial slip and the formation of planar defects dominates, but austenitic slip systems with

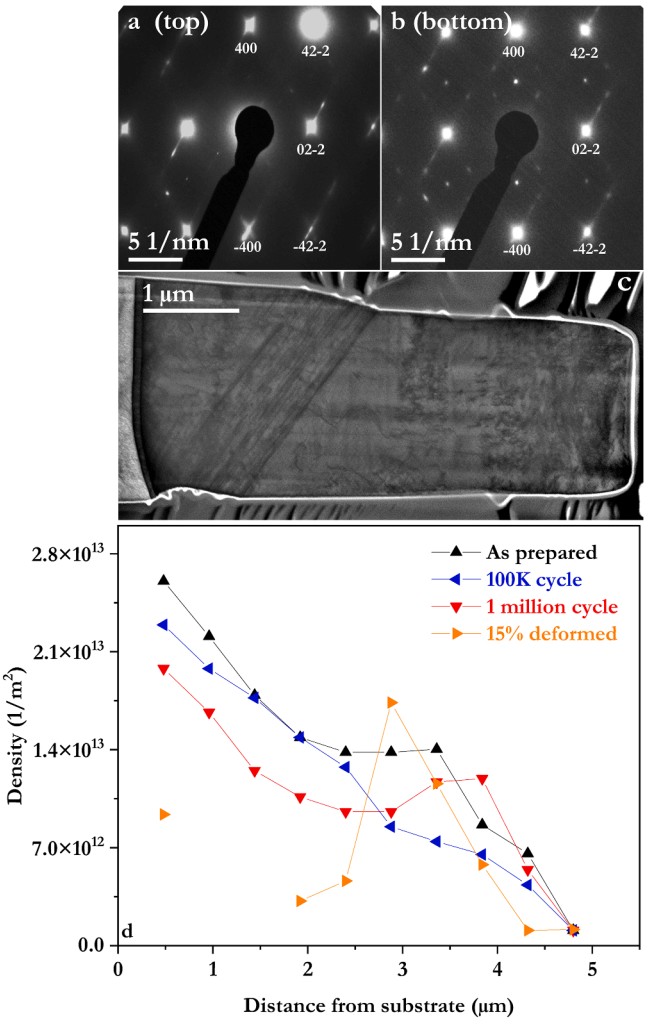

Fig. 9. Transmission electron micrographs of a microcrystal after 15% plastic deformation. A slip band passing through the lower region of the microcrystal can be seen in the BF-STEM image (c). Diffraction patterns obtained from the upper and lower regions of the column are show respectively in (a, b). (d) Dislocation density as a distance from the substrate for all microcrystals studied. (c) was intentionally rotated such that the microcrystal length matches the abscissa and distance from the substrate in (d).

small barriers energies will already contribute to dislocation nucleation and glide in the superelastic stress domain. With slip in Ni-Mn-Ga being restricted to the high-stress regime of the martensite, functional fatigue, as observed and further discussed in the following, must indeed be limited.

4.2. Loss-free phase transformations at the micron scale

In comparison to their bulk counterparts (of composition $Ni_{52}Mn_{24.4}Ga_{23.6}$ [6]), all as-prepared microcrystals reveal a significantly increased transformation stress, being approximately two times larger when correcting for the temperature offset relative to M_s via the Clausius-Clapeyron equation. This stands in direct contrast with recent observations obtained from polycrystalline bulk $Ni_{51}Mn_{28}Ga_{21}$ (instead of the here investigated $Ni_{51.3}Mn_{21.7}Ga_{27}$), where a transformation stress of extracted microcrystals with a diameter of 1 µm exhibited a very similar value of ca. 230 MPa as for the corresponding bulk material [23]. Given the findings in Fig. 6 and the unclear initial microstructural condition of the microcrystals in Ref. [23], we argue that this discrepancy in transformation stress may originate from subtle differences in the pre-existing defect structure. Indeed, our data shows that the transformation stress, if determined from the second derivative of the stress-strain response, exhibits a gradual decrease after plastic-pre-straining. As summarized in Fig. 6, increasing amounts of plastic deformation reduces the transformation stress and after about 17% plastic strain, the inflection of the superelastic stress-strain curve has vanished. Yet, elastic strains of about 4% are still admitted by the microcrystals. Since the plastic pre-straining introduces a pronounced dislocation structure in the samples, as also shown in Fig. 9, we conclude that an accumulation of lattice distortions via dislocations facilitates the martensitic nucleation, which has earlier been discussed for Cu-Al-Ni in Ref. [67], further proposing that dislocation cores already provide sufficient atomic pre-shearing in the direction for martensitic nucleation. Given that no residual martensite could be identified via TEM in plastically deformed samples, it follows that the phase-transformation stress eventually becomes vanishingly small, while the 4% reversible strain must originate from twin-boundary motion in the formed martensite. In view of the higher and size-effected transformation stress of the microcrystals in comparison to the bulk scale, pre-existing defects arise as a factor that can strongly affect the materials transformation stress. At the same time, this implies that pre-existing defect structures or plastic straining emerge as possible avenues to tune the transformation stress to a desired value.

Evaluation of the enclosed stress-strain hysteresis during superelastic switching reveals an almost loss-free response, with a dissipation energy of the order of 0.5–1 MJ/m^3. This holds true for the first phase-transformation cycle, as well as for the 10^6th cycle, the latter of which exhibits at most a reduction in the reversible strain magnitude of about 2.5% if cycled between 0 and approximately 8×10^5 cycles. As such, functional fatigue, as known for Ni-Ti [24], is essentially absent in Ni-Mn-Ga. This loss-free superelastic behavior persists even after plastic pre-deformation, demonstrating how dislocation structures, extensive slip, and local lattice rotations do not affect the superelastic behavior. Together with findings of magnetic phase-switching of Ni-Mn-Ga bulk crystals [68–70], the here demonstrated lack of microstructural and mechanical dissipation, even after predeformation, demonstrates an exceptionally reversibility and robustness of Ni-Mn-Ga as a SMA.

Whilst is it challenging to define a clear microstructural origin of this degradation-free superelasticity, it is instructive to consider the concept of a transformation stretch tensor as discussed by Cui et al. [71]. This theory of reversible phase transformation relies on local lattice compatibility between the austenitic phase and the possible martensitic variants. Considering a cubic to orthorhombic transformation and six possible variants that form via a face-diagonal stretch, the transformation stretch tensor becomes $U = f(a,b,c)$, where $\alpha = \frac{a}{a_o}, \beta = \frac{b}{a_o}, \gamma = \frac{c}{a_o}$, and a_0 is the lattice parameter of the cubic austenite and a, b, c are the lattice parameters of the orthorhombic martensite. As shown elsewhere [71], all six transformation stretch tensors have the same eigenvalues λ_2, making it sufficient to evaluate the required conditions for a completely loss-free superelastic hysteresis once. These are $\det(U) = 1$ for no volume change during the transformation and $\lambda_2 = 1$, signifying a full compatibility of the austenite with a single variant of martensite.

With appropriate lattice constants for both phases, these conditions can be evaluated for the present case and exemplarily compared to low-loss SMAs in Refs. [72,73,75]. Table 1 lists the used parameters and resulting $\det(U)$ and λ_2, demonstrating how $Ni_{51.3}Mn_{21.7}Ga_{27}$ has the closest to ideal condition for all considered cases. We note that this evaluation relies on defect-free lattices, which clearly is not the case for the investigated microcrystals. Both the grown-in threading dislocations and the premartensitic structure in the as-prepared samples, as well as dislocation structures in the pre-deformed crystals will contribute to considerable deviations from this ideal case. Whilst dislocations may locally induce both positive and negative deviations relative to the ideal case, the extensive signature of horizontal premartensitic domains are expected to favor the compatibility condition. Based on the transformation stretch tensor framework, one would therefore expect even

Table 1
a, b, c, and a_0 represent the lattice constants of martensite and austenite. Both the first and second conditions are calculated using these lattice constants. To compare Ni-Mn-Ga austenite-martensite compatibility, the data from the literature is also taken for comparison.

a	b	c	a_0	Det U_1	λ_2	Composition	References
0.618	0.578	0.562	0.578	1.044	1.099	$Ni_{54.8}Mn_{22.0}Ga_{23.2}$	[72]
0.616	0.579	0.548	0.581	1.003	1.124	$Ni_{51.2}Mn_{24.6}Ga_{24.2}$	[73,74]
0.609	0.578	0.554	0.582	0.993	1.099	$Ni_{52}Mn_{23}Ga_{25}$	[75]
0.38	0.38	0.32	0.286	2.004	1.187	$Co_{49}Ni_{22}Ga_{29}$	[11]
0.614	0.583	0.550	0.583	1.008	1.08	$Ni_{51}Mn_{22}Ga_{27}$	Present work

closer values to unity for both $\det(U)$ and λ_2. Being at this point purely hypothetical considerations, one has to acknowledge that the enclosed superelastic envelopes remain, within the experimental resolution, very similar for both the as-prepared and pre-deformed microcrystals. As such, the considerably lower loss than in the bulk counterpart must be primarily due to the as-prepared crystal state with its considerable premartensitic lattice fraction and not due to dislocation structures.

5. Summary

In support of future functional applications of Ni-Mn-Ga shape-memory alloys at the small-scale, we investigate here the micro-mechanical behavior during stress-driven superelastic cycling up to 10^6 phase-transformation cycles. Microstructural characterization using transmission-electron microscopy complement the assessment of the material's functional fatigue. The following core conclusions can be made:

- Up to one million superelastic cycles, functional fatigue, expressed as a relative reduction of the initial switching strain, amounts to ca. 2–3%, demonstrating an outstanding robustness during mechanically-driven phase transformations.
- This degradation-free superelastic behavior persists also in the presence of introduced initial dislocation structures and slip bands.
- With increasing amount of plastic prestrain, a reduction of the phase-transformation stress is observed.
- No evidence of residual martensite can be identified after 10^6 switching cycles in the as-prepared microcrystals, which also applies to cycled but pre-deformed microcrystals.
- Hysteresis envelopes of the cycled microcrystals enclose a dissipative response that is approximately 20% of the corresponding bulk signal, whereas the transformation stress is approximately twice its bulk value.
- The microcrystals deform plastically in the range of 1–1.4 GPa, leading to a strongly size-affected stress range for mechanical switching.

These findings show the outperforming functional robustness of Ni-Mn-Ga in comparison to, for example Ni-Ti or Au-Cu-Zn [76], and reveal for the first time the stability of the superelastic behavior up to the million-cycle switching domain. Whilst a size effect in the transformation stress is observed, the introduction of dislocations via plastic straining suggests a full tunability of the transformation stress without any deterioration of the functional performance. Together, these results underline the high promise of Ni-Mn-Ga as a candidate material for small-scale actuation in nano- or micro-electro-mechanical devices.

CRediT authorship contribution statement

Adnan Fareed: Data curation, Formal analysis, Investigation, Writing – original draft. **Julian M. Rosalie:** Formal analysis, Investigation, Visualization, Writing – original draft. **Satyakam Kar:** Formal analysis, Resources, Writing – review & editing. **Sebastian Fähler:** Conceptualization, Funding acquisition, Supervision, Writing – review & editing. **Robert Maaß:** Conceptualization, Funding acquisition, Methodology, Project administration, Resources, Supervision, Validation, Writing – original draft, Writing – review & editing.

Declaration of competing interest

The authors declare that they have no known competing financial interests or personal relationships that could have appeared to influence the work reported in this paper.

Acknowledgements

A.F. thanks R. Hesse, BAM, for support and training in the Focus ion beam method. R.M. is grateful for financial support from the BAM-IFW (Grant No. MIT1-20-63-IFW) funding scheme and for institutional support from the Federal Institute of Materials Research and Testing (BAM). The authors would also like to thank H. Reith from IFW for supporting the film processing and O. Schwarze from BAM for his support of the used nanoindentation device. This research was carried out in part at the electron microscopy center at BAM.

References

[1] N. Choudhary, D. Kaur, Shape memory alloy thin films and heterostructures for MEMS applications: a review, Sens. Actuators A Phys. 242 (2016) 162–181.
[2] H.E. Karaca, I. Karaman, B. Basaran, Y.J. Chumlyakov, H.J. Maier, Magnetic field and stress induced martensite reorientation in NiMnGa ferromagnetic shape memory alloy single crystals, Acta Mater. 54 (2006) 233–245.
[3] W. Huang, On the selection of shape memory alloys for actuators, Mater. Des. 23 (2002) 11–19.
[4] M. Arndt, M. Griebel, V. Novák, T. Roubícek, P. Sittner, Martensitic transformation in NiMnGa single crystals: numerical simulation and experiments, Int. J. Plast. 22 (2006) 1943–1961.
[5] H.E. Karaca, I. Karaman, D.C. Lagoudas, H.J. Maier, Y.I. Chumlyakov, Recoverable stress-induced martensitic transformation in a ferromagnetic CoNiAl alloy, Scr. Mater. 49 (2003) 831–836.
[6] V.A. Chernenko, J. Pons, E. Cesari, K. Ishikawa, Stress-temperature phase diagram of a ferromagnetic Ni-Mn-Ga shape memory alloy, Acta Mater. 53 (2005) 5071–5077.
[7] B. Strnadel, S. Ohashi, H. Ohtsuka, S. Miyazaki, Effect of mechanical cycling on the pseudoelasticity characteristics of Ti-Ni and Ti-Ni-Cu alloys, Mater. Sci. Eng. A Struct. 203 (1995) 187–196.
[8] S. Miyazaki, H.Y. Kim, H. Hosoda, Development and characterization of Ni-free Ti-base shape memory and superelastic alloys, Mater. Sci. Eng. A 438-440 (2006) 18–24.
[9] J. Ma, B.C. Hornbuckle, I. Karaman, G.B. Thompson, Z.P. Luo, Y.I. Chumlyakov, The effect of nanoprecipitates on the superelastic properties of FeNiCoAlTa shape memory alloy single crystals, Acta Mater. 61 (2013) 3445–3455.
[10] Y.I. Chumlyakov, Orientational dependence of shape memory effects and superelasticity in CoNiGa, NiMnGa, CoNiAl, FeNiCoTi, and TiNi single crystals, Russ. Phys. J. 97 (2004) 893–911.
[11] V.A. Chernenko, J. Pons, E. Cesari, I.K. Zasimchuk, Transformation behaviour and martensite stabilization in the ferromagnetic Co–Ni–Ga Heusler alloy, Scr. Mater. 50 (2004) 225–229.
[12] K.F. Xu, J. Luo, C. Li, Y.L. Shen, C.J. Li, X. Ma, M.Q. Li, Mechanisms of stress-induced martensitic transformation and transformation-induced plasticity in NiTi shape memory alloy related to superelastic stability, Scr. Mater. 217 (2022) 1–6.
[13] J. Michutta, M.C. Carroll, A. Yawny, C. Somsen, K. Neuking, G. Eggeler, Martensitic phase transformation in Ni-rich NiTi single crystals with one family of Ni_4Ti_3 precipitates, Mater. Sci. Eng. A Struct. 378 (2004) 152–156.
[14] L. Heller, P. Sittner, P. Sedlák, H. Seiner, O. Tyc, L. Kaderávek, P. Sedmák, M. Vronka, Beyond the strain recoverability of martensitic transformation in NiTi, Int. J. Plast. 116 (2019) 232–264.
[15] R. Maaß, P.M. Derlet, Micro-plasticity and recent insights from intermittent and small-scale plasticity, Acta Mater. 143 (2018) 338–363.
[16] D.C. Dunand, P. Mullner, Size effects on magnetic actuation in Ni-Mn-Ga shape-memory alloys, Adv. Mater. 23 (2011) 216–232.

[17] J. San Juan, M.L. No, C.A. Schuh, Nanoscale shape-memory alloys for ultrahigh mechanical damping, Nat. Nanotechnol. 4 (2009) 415–419.
[18] C.P. Frick, S. Orso, E. Arzt, Loss of pseudoelasticity in nickel-titanium sub-micron compression pillars, Acta Mater. 55 (2007) 3845–3855.
[19] C.P. Frick, B.G. Clark, A.S. Schneider, R. Maass, S. Van Petegem, H. Van Swygenhoven, On the plasticity of small-scale nickel-titanium shape memory alloys, Scr. Mater. 62 (2010) 492–495.
[20] J. San Juan, M.L. Nó, C.A. Schuh, Thermomechanical behavior at the nanoscale and size effects in shape memory alloys, J. Mater. Res. 26 (2011) 2461–2469.
[21] J. San Juan, M.L. Nó, C.A. Schuh, Superelasticity and shape memory in micro- and nanometer-scale pillars, Adv. Mater. 20 (2007) 272–278.
[22] V. Fuster, J.F. Gómez-Cortés, M.L. Nó, J.M. San Juan, Universal scaling law for the size effect on superelasticity at the nanoscale promotes the use of shape-memory alloys in stretchable devices, Adv. Electron. Mater. 6 (2020) 1900741.
[23] J.F. Gómez-Cortés, P. Czaja, M.L. Nó, M.J. Szczerba, J.M. San Juan, Extremely stable stress-induced martensitic transformation at the nanoscale during superelastic cycling of Ni51Mn28Ga21 shape memory alloy, Mater. Sci. Eng. A 881 (2023) 145339.
[24] P. Hua, K.J. Chu, F.Z. Ren, Q.P. Sun, Cyclic phase transformation behavior of nanocrystalline NiTi at microscale, Acta Mater. 185 (2020) 507–517.
[25] O. Heczko, H. Seiner, S. Fähler, Coupling between ferromagnetic and ferroelastic transitions and ordering in Heusler alloys produces new multifunctionality, MRS Bull. 47 (2022) 618–627.
[26] A. Sozinov, N. Lanska, A. Soroka, W. Zou, 12% magnetic field-induced strain in Ni-Mn-Ga-based non-modulated martensite, Appl. Phys. Lett. 102 (2013) 021902.
[27] A. Backen, S.R. Yeduru, A. Diestel, L. Schultz, M. Kohl, S. Fähler, Epitaxial Ni-Mn-Ga films for magnetic shape memory alloy microactuators, Adv. Eng. Mater. 14 (2012) 696–709.
[28] A. Sozinov, A.A. Likhachev, N. Lanska, K. Ullakko, Giant magnetic-field-induced strain in NiMnGa seven-layered martensitic phase, Appl. Phys. Lett. 80 (2002) 1746–1748.
[29] S. Fähler, Caloric effects in ferroic materials: new concepts for cooling, Energy Technol. 6 (2018) 1394–1396.
[30] T. Gottschall, A. Gracia-Condal, M. Fries, A. Taubel, L. Pfeuffer, L. Manosa, A. Planes, K.P. Skokov, O. Gutfleisch, A multicaloric cooling cycle that exploits thermal hysteresis, Nat. Mater. 17 (2018) 929–934.
[31] M. Kohl, M. Gueltig, F. Wendler, Coupled simulation of thermomagnetic energy generation based on NiMnGa Heusler alloy films, Shape Mem. Superelast. 4 (2018) 242–255.
[32] M. Gueltig, F. Wendler, H. Ossmer, M. Ohtsuka, H. Miki, T. Takagi, M. Kohl, High-performance thermomagnetic generators based on Heusler alloy films, Adv. Energy Mater. 7 (2016) 1–7.
[33] X. Fu, C. Liu, X. Lu, X. Li, J. Lv, F. Wang, L. Wang, Nanoscale mechanical properties of nanoindented Ni(48.8)Mn(27.2)Ga(24) ferromagnetic shape memory thin film, Scanning 2017 (2017) 4630156.
[34] A. Fareed, J.M. Rosalie, S. Kumar, S. Kar, T. Hickel, S. Fähler, R. Maass, Constrained incipient phase transformation in Ni-Mn-Ga films: a small-scale design challenge, Mater. Des. 233 (2023) 112259.
[35] S. Kar, Y. Ikeda, K. Lünser, T.G. Woodcock, K. Nielsch, H. Reith, R. Maass, S. Fähler, Growth twins and premartensite microstructure in epitaxial Ni-Mn-Ga films, Acta Mater. 252 (2023) 118902.
[36] S. Schwabe, R. Niemann, A. Backen, D. Wolf, C. Damm, T. Walter, H. Seiner, O. Heczko, K. Nielsch, S. Fähler, Building hierarchical martensite, Adv. Funct. Mater. 31 (2020) 1–11.
[37] R. Maaß, C.A. Volkert, P.M. Derlet, Crystal size effect in two dimensions–influence of size and shape, Scr. Mater. 102 (2015) 27–30.
[38] H. Zhang, B.E. Schuster, Q. Wei, K.T. Ramesh, The design of accurate micro-compression experiments, Scr. Mater. 54 (2006) 181–186.
[39] S. Shim, H. Bei, M.K. Miller, G.M. Pharr, E.P. George, Effects of focused ion beam milling on the compressive behavior of directionally solidified micropillars and the nanoindentation response of an electropolished surface, Acta Mater. 57 (2009) 503–510.
[40] D.C. Jang, R. Maass, G.Y. Wang, P.K. Liaw, J.R. Greer, Fatigue deformation of microsized metallic glasses, Scr. Mater. 68 (2013) 773–776.
[41] R. Hull, J.C. Bean, Misfit dislocations in lattice-mismatched epitaxial films, Crit. Rev. Solid State Mater.Sci. 17 (1992) 507–546.
[42] S.E. Bennett, Dislocations and their reduction in GaN, Mater. Sci. Technol. 26 (2010) 1017–1028.
[43] I.M. Robertson, C.M. Wayman, Tweed microstructures I. Characterization in β-NiAl, Philos. Mag. A 48 (2006) 421–442.
[44] S.M. Shapiro, B.X. Yang, G. Shirane, Y. Noda, L.E. Tanner, Neutron scattering study of the martensitic transformation in a Ni-Al beta -phase alloy, Phys. Rev. Lett. 62 (1989) 1298–1301.
[45] S.M. Shapiro, Y. Noda, Y. Fujii, Y. Yamada, X-ray investigation of the premartensitic phase inNi46.8Ti50Fe3.2, Phys. Rev. B 30 (1984) 4314–4321.
[46] M.B. Salamon, M.E. Meichle, C.M. Wayman, Premartensitic phases of Ti50Ni47Fe3, Phys. Rev. B Condens. Matter 31 (1985) 7306–7315.
[47] R. Oshima, M. Sugiyama, F.E. Fujita, Tweed structures associated with Fcc-Fct transformations in Fe-Pd alloys, Metall. Trans. A 19 (1988) 803–810.
[48] S. Muto, R. Oshima, F.E. Fujita, Elastic softening and elastic strain energy consideration in the f.c.c.–f.c.t. transformation of Fe Pd alloys, Acta Metall. Mater. 38 (1990) 685–694.
[49] L. Righi, F. Albertini, E. Villa, A. Paoluzi, G. Calestani, V. Chernenko, S. Besseghini, C. Ritter, F. Passaretti, Crystal structure of 7M modulated Ni-Mn-Ga martensitic phase, Acta Mater. 56 (2008) 4529–4535.
[50] L. Righi, F. Albertini, L. Pareti, A. Paoluzi, G. Calestani, Commensurate and incommensurate "5M" modulated crystal structures in Ni-Mn-Ga martensitic phases, Acta Mater. 55 (2007) 5237–5245.
[51] P.J. Brown, J. Crangle, T. Kanomata, M. Matsumoto, K.-U. Neumann, B. Ouladdiaf, K.R.A. Ziebeck, The crystal structure and phase transitions of the magnetic shape memory compound Ni2MnGa, J. Phys. Condens. Matter 14 (2002) 10159–10171.
[52] D. Kiener, C. Motz, M. Rester, M. Jenko, G. Dehm, FIB damage of Cu and possible consequences for miniaturized mechanical tests, Mater. Sci. Eng. A 459 (2007) 262–272.
[53] R. Maaß, S. Van Petegem, C.N. Borca, H. Van Swygenhoven, *In situ* Laue diffraction of metallic micropillars, Mater. Sci. Eng. A 524 (2009) 40–45.
[54] I.R. Aseguinolaza, E. Modin, A. Chuvilin, J.M. Barandiaran, V.A. Chernenko, Submicron pillars of ferromagnetic shape memory alloys: thermomechanical behavior, Appl. Mater. Today 12 (2018) 9–14.
[55] J.P. McCaffrey, Surface damage formation during ion-beam thinning of samples for transmission electron microscopy, Ultramicroscopy 87 (2001) 97–104.
[56] R. Maass, L. Meza, B. Gan, S. Tin, J.R. Greer, Ultrahigh strength of dislocation-free Ni_3Al nanocubes, Small 8 (2012) 1869–1875.
[57] S. Kar, K. Nielsch, S. Fähler, H. Reith, Microfabrication approaches on magnetic shape memory films, Adv. Eng. Mater. 25 (2023) 2301133. -2301131-2301110.
[58] M. Kök, Y. Aydoğdu, Effect of composition on the thermal behavior of NiMnGa alloys, J. Therm. Anal. Calorim. 113 (2012) 859–863.
[59] M.D. Uchic, P.A. Shade, D.M. Dimiduk, Plasticity of micrometer-scale single crystals in compression, Annu. Rev. Mater. Res. 39 (2009) 361–386.
[60] G. Sparks, R. Maass, Nontrivial scaling exponents of dislocation avalanches in microplasticity, Phys. Rev. Mater. 2 (2018) 120601.
[61] R. Maaß, M.D. Uchic, *In-situ* characterization of the dislocation-structure evolution in Ni micro-pillars, Acta Mater. 60 (2012) 1027–1037.
[62] G.E. Lakso, M. Marcinkowski, Plastic deformation behavior in the Fe_3Si superlattice, Trans. Metall. Soc. AIME 245 (1969) 1111–1120.
[63] Green, Plastic deformation of single crystals of the Heusler alloy Cu_2MnAl, Metall. Trans. A 8A (1977) 353–361.
[64] P.M. Derlet, R. Maaß, Universal power-law strengthening in metals? Scr. Mater. 109 (2015) 19–22.
[65] J.F. Gomez-Cortes, M.L. No, I. Lopez-Ferreno, J. Hernandez-Saz, S.I. Molina, A. Chuvilin, J.M. San Juan, Size effect and scaling power-law for superelasticity in shape-memory alloys at the nanoscale, Nat. Nanotechnol. 12 (2017) 790–796.
[66] P. Chowdhury, H. Sehitoglu, A revisit to atomistic rationale for slip in shape memory alloys, Prog. Mater. Sci. 85 (2017) 1–42.
[67] A. Ibarra, D. Caillard, J. San Juan, M.L. Nó, Martensite nucleation on dislocations in Cu-Al-Ni shape memory alloys, Appl. Phys. Lett. 90 (2007) 1–3.
[68] I. Aaltio, A. Soroka, Y. Ge, O. Söderberg, S.P. Hannula, High-cycle fatigue of 10M Ni-Mn-Ga magnetic shape memory alloy in reversed mechanical loading, Smart Mater. Struct. 19 (2010) 075014.
[69] M. Chmielus, X.X. Zhang, C. Witherspoon, D.C. Dunand, P. Mullner, Giant magnetic-field-induced strains in polycrystalline Ni-Mn-Ga foams, Nat. Mater. 8 (2009) 863–866.
[70] Y. Boonyongmaneerat, M. Chmielus, D.C. Dunand, P. Mullner, Increasing magnetoplasticity in polycrystalline Ni-Mn-Ga by reducing internal constraints through porosity, Phys. Rev. Lett. 99 (2007) 247201.
[71] J. Cui, Y.S. Chu, O.O. Famodu, Y. Furuya, J. Hattrick-Simpers, R.D. James, A. Ludwig, S. Thienhaus, M. Wuttig, Z. Zhang, I. Takeuchi, Combinatorial search of thermoelastic shape-memory alloys with extremely small hysteresis width, Nat. Mater. 5 (2006) 286–290.
[72] S. Kaufmann, U.K. Rossler, O. Heczko, M. Wuttig, J. Buschbeck, L. Schultz, S. Fahler, Adaptive modulations of martensites, Phys. Rev. Lett. 104 (2010) 145702.
[73] Y. Ge, O. Heczko, S.P. Hannula, S. Fähler, Probing structure and microstructure of epitaxial Ni-Mn-Ga films by reciprocal space mapping and pole figure measurements, Acta Mater. 58 (2010) 6665–6671.
[74] J. Buschbeck, R. Niemann, O. Heczko, M. Thomas, L. Schultz, S. Fähler, *In situ* studies of the martensitic transformation in epitaxial Ni–Mn–Ga films, Acta Mater. 57 (2009) 2516–2526.
[75] M. Thomas, O. Heczko, J. Buschbeck, U.K. Rössler, J. McCord, N. Scheerbaum, L. Schultz, S. Fähler, Magnetically induced reorientation of martensite variants in constrained epitaxial Ni-Mn-Ga films grown on MgO(001), New J. Phys. 10 (2008) 023040.
[76] X. Ni, J.R. Greer, K. Bhattacharya, R.D. James, X. Chen, Exceptional resilience of small-scale $Au_{30}Cu_{25}Zn_{45}$ under cyclic stress-induced phase transformation, Nano Lett. 16 (2016) 7621–7625.